Nano Research

Open Access

Research Article

Mechanochemical graphene exfoliation with succinic acid to confine Ni nanoclusters for electrochemical nitrate reduction

Nitin Goyal[1], Zelong Zheng[1], Wenjie Lin[1], Fei Li[1], Sateesh Bandaru[3] ✉, and Yi-bo Hu[1,2] ✉

[1] *Xiamen Key Laboratory of Municipal and Industrial Solid Waste Utilization and Pollution Control, College of Civil Engineering, Huaqiao University, Xiamen 361021, China*
[2] *School of Environmental Science and Engineering, Shanghai Jiao Tong University, Shanghai 200240, China*
[3] *Institute of Advanced Magnetic Materials, College of Materials and Environmental Engineering, Hangzhou Dianzi University, Hangzhou 310012, China*

Cite this article: *Nano Research*, **2026**, *19*, 94908824. https://doi.org/10.26599/NR.2026.94908824

ABSTRACT: Developing a sustainable synthesis method for functionalized graphene remains in a great demand. In this work, we developed a mechanochemical method for graphene production from graphite with succinic acid as the functionalization agent. Succinic acid effectively functionalized the surface of graphite with oxygen containing groups with the mechanical energy generated during ball milling, resulting in smooth exfoliation of graphene sheets. Density functional theory (DFT) and *ab initio* molecular dynamics (AIMD) simulations calculations revealed that the intact carboxyl –COOH group of the succinic acid interacts most favorably with the graphene surface, exhibiting a significantly lower adsorption energy barrier compared to the epoxyl >O and hydroxyl –OH groups. This result helps understand the thermodynamically predominant role of –COOH group in the functionalization and exfoliation process. On the other hand, the enriched oxygen groups provide abundant nucleation sites, obtaining smaller Ni nanoclusters (8–10 nm) on the graphene. Using the exfoliated graphene doped with highly dispersed Ni nanoclusters for electrochemical nitrate reduction yielded an outstanding ammonia production rate of 12.9 mg·cm^{-2}·h^{-1} at −1.0 V versus reversible hydrogen electrode (RHE), with remarkable Faradaic efficiency of 90% and selectivity of 78%. Overall, this study establishes a sustainable and scalable method to synthesize functionalized graphene for efficient electrochemical conversion from nitrate to ammonia.

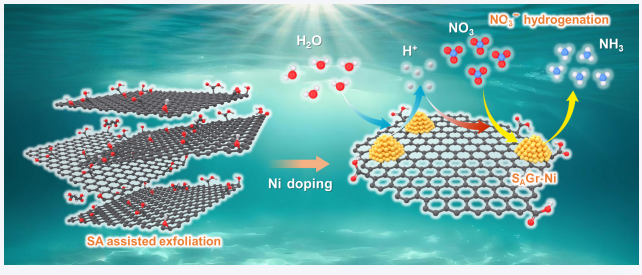

KEYWORDS: graphene, ball milling, exfoliation, succinic acid, nitrate reduction

1 Introduction

Graphene is a single-atom-thick sheet of carbon atoms organized in a hexagonal lattice, exhibiting outstanding electrical and thermal conductivities, superior mechanical strength, and an extensive specific surface area [1]. These attributes make graphene a promising candidate for diverse applications including energy storage [2], electrocatalysis [3], gas separation [4], sensors [5], and environmental remediation [6]. Established methods like chemical vapor deposition (CVD) and electrochemical exfoliation are hampered by tedious processes and high operational expenses [7], while chemical oxidation routes like the Hummers' method rely on corrosive reagents that generate substantial environmental hazards [8]. In addition, the potential of graphene is hindered by both the limitations of its scalable and sustainable synthesis as its sheets restack via strong π–π and van der Waals interactions, highlighting the need for controllable fabrication strategies [9]. This structural challenge becomes particularly unfavorable in reactions such as electrochemical nitrate (NO_3^-) reduction to ammonia (NH_3), where maximizing active site exposure and efficient electron transfer are essential for achieving high selectivity and Faradaic efficiency (FE) [10]. Overcoming graphene restacking through controlled surface functionalization and the incorporation of catalytically active metal nanoclusters [11] represents a crucial step towards selective conversion of NO_3^- to NH_3 and other applications as well [12].

Mechanochemical ball milling has recently attracted attention as a simple, scalable, and sustainable approach for producing high-quality graphene sheets by delaminating graphite through shear forces while largely preserving the integrity of the basal plane [13].

Received: February 27, 2026; **Revised:** April 19, 2026
Accepted: May 8, 2026

✉Address correspondence to Yi-bo Hu, hybhqu@hqu.edu.cn; Sateesh Bandaru, sbandaru@hdu.edu.cn

However, this mechanochemical approach needs for precise control over surface chemistry, which is essential for creating stable anchoring sites for metal nanoclusters. Several additives such as dry ice [14] oxalic acid, malic acid, tartaric acid [15], and xylitol [16] have been explored to assist in the milling process. However, it has been observed that these additives often exhibit poor exfoliation efficiency because their hydrogen-bonding interactions with graphite are insufficient to overcome the strong van der Waals forces between graphene layers [17–20].

Succinic acid (SA), a United States Department of Agriculture (USDA) certified bio-based compound [21], which can serve a dual role during high-energy ball milling with stainless steel balls. Its dicarboxylic groups act as "molecular scissors", simultaneously promoting graphite exfoliation and functionalizing the graphene lattice with oxygen-containing groups (=O, –OH, and –COOH). This strategy generates abundant edge sites and tailored defects without damaging the basal plane, effectively minimizing π–π restacking. Furthermore, oxygen-containing functional groups enhance the graphene surface affinity toward metal precursors [22], enabling strong coordination and electrostatic interactions with metal ions. These sites act as nucleation centers, yielding uniformly dispersed metal-based nanoclusters [23, 24].

Herein, we report the synthesis of succinic acid-functionalized graphene (S_AGr) via a one-step mechanochemical ball milling process. Afterwards, Ni nanoclusters were uniformly doped on the S_AGr. Raman spectroscopy, X-ray photoelectron spectroscopy (XPS), and high-resolution transmission electron microscopy (HR-TEM) were employed to investigate the speciation of oxygen-containing groups and their role in modulating the electronic structure of Ni. Additionally, a combination of density functional theory (DFT) and *ab initio* molecular dynamics (AIMD) simulations provided deep insights into the adsorption behavior and interaction pathways of succinic acid on the graphene surface, revealing its crucial role in initiating functionalization and exfoliation. Electrochemical analyses confirm that S_AGr-Ni exhibits excellent ammonia production rate of 12.9 $mg{\cdot}h^{-1}{\cdot}cm^{-2}$ with a selectivity of 78%. Furthermore, tert-butanol (TBA) quenching experiments were performed to confirm the key role of H^* species, as increased TBA dosage markedly inhibits nitrate reduction. This study reports a novel strategy to produce functionalized graphene, where oxygen-containing groups promote uniform dispersion of metal cluster approximately 8–10 nm and enable efficient electrochemical reduction of NO_3^- to NH_3.

2 Experimental section

2.1 Synthesis of Gr-Ni and S_AGr-Ni

The chemicals used in the experiments are summarized in the Electronic Supplementary Material (ESM). Initially, pristine graphite was subjected to mechanochemical ball milling at 500 rpm for 48 h using 3 mm stainless steel balls with a powder to ball mass ratio of 1:25 [25]. The milling process was operated in a cyclic mode for 25 min of milling followed by 5 min of interval. The milled product was thoroughly washed with 0.5 L of deionized (DI) H_2O and dried at 70 °C to obtain graphene denoted as Gr. To prepare the functionalized support, graphite and $C_4H_6O_4$ were combined in a mass ratio of 1:2 and milled under identical conditions like Gr. The resulting solid was washed with 0.5 L of DI H_2O and dried at 70 °C to yield succinic acid functionalized graphene denoted as S_AGr. For catalyst preparation, 100 mg of each support was dispersed in 45 mL of C_2H_5OH containing 100 mg of CH_4N_2O and 10 mg of $NiCl_2.6H_2O$. The suspension was ultrasonicated for 90 min and magnetically stirred at 650 rpm for 16 h to ensure homogeneous precursor distribution. Subsequently hydrothermal treatment was carried out at 180 °C for 12 h. The obtained material was washed, dried, and subjected to pyrolysis at 700 °C for 2 h under N_2 atmosphere with a heating rate of 10 $°C{\cdot}min^{-1}$ to prepare the final catalysts denoted as Gr-Ni and S_AGr-Ni.

2.2 Characterization

The comprehensive structural and physicochemical characterizations were performed and detailed descriptions of the instrumentation and experimental conditions are provided in the ESM.

2.3 Electrochemical NO_3^- reduction

The electrochemical experiments were conducted in a Gaoss Union H-shaped electrolytic cell using a direct current (DC) power supply as the power source. 80 mL of solution containing 1 M NaOH was placed in the anode chamber, while 80 mL of 0.1 M $NaNO_3$ and 1–2 mL of 1 M NaOH to maintain the pH of 12.5 were added to the cathode chamber. A platinum electrode and Ag/AgCl were used as the counter and reference electrodes, respectively. Carbon paper (2 cm × 2 cm) served as the working electrode. Nafion N117 proton exchange membrane was pretreated by boiling it in 5 wt.% H_2O_2 and 5 wt.% H_2SO_4. Initially, the carbon paper was washed with ethyl alcohol and water before use. Subsequently, 3 mg of catalyst was dispersed in 0.2 mL of Nafion solution, 0.1 mL of ethyl alcohol, and 0.2 mL of DI water and sonicated for 60 min. Then, 30 μL of the catalyst ink was deposited onto the carbon paper and left to dry for 30 min in the ambient conditions. The linear sweep voltammetry (LSV) curves and chronoamperometry were performed on the CHI 660E electrochemical instrumentation (Shanghai CH Instruments, Inc.). Cyclic voltammetry (CV) measurements were conducted in the cathodic chamber containing 1 M NaOH with 0.1 M NO_3^- over a potential large window of –0.9–+0.9 V vs. reversible hydrogen electrode (RHE) to probe surface hydrogen adsorption behavior relevant to nitrate reduction. All quantitative experiments were carried out in triplicate, and the error bars are provided.

Additionally, the NO_2^-, NO_3^-, and NH_3 concentrations were determined from standard calibration curves, as described in the ESM. Detailed measurement procedures and the corresponding calculations for ammonia yield rate, Faradaic efficiency, and selectivity are provided in the ESM.

Ammonia was quantified using ^1H nuclear magnetic resonance (NMR) spectroscopy at 500 MHz with maleic acid as an internal standard. The standard solutions of $^{15}NH_4Cl$ with concentrations of 10, 20, 30, 40, and 50 mM were prepared, and a fixed amount of maleic acid was dissolved in each 10 mL of solution. The pH was adjusted to 2 by adding 150 μL of 3 wt.% HCl, and D_2O was introduced for signal locking. The identical protocol was used for the $^{14}NH_4Cl$ control sample to enable direct comparison with the $^{15}NH_4^+$ product. The calibration curve was constructed using the integral area ratio of $^{15}NH_4^+$ to maleic acid, as shown in Figs. S11(a) and S11(b) in the ESM. Subsequently, 200 mg of $^{15}NO_3^-$ was used in the cathodic chamber of an H-cell. After 1 h of electrolysis, the sample was collected, the pH was adjusted to 2, and the solution was sealed in an NMR tube for measurements.

2.4 DFT study of graphene exfoliation and free energy calculations for the NO_3^- reduction pathway

All calculations were performed using DFT within the Vienna *ab initio* simulation package (VASP) [26, 27]. The exchange-correlation interactions were described by the Perdew–Burke–Ernzerhof (PBE) generalized-gradient approximation (GGA), with van der Waals corrections accounted for using the DFT-D3 method [28]. A periodic slab model was constructed to simulate the interaction of succinic acid with graphene. The model consisted of a four-layer graphene slab and a pre-optimized succinic acid molecule. The supercell had lattice constants of 9.87 and 17.09 Å along the "*a*" and "*b*" axes, respectively, with a vacuum layer of 15 Å added along the "*c*" axis to prevent spurious interactions between periodic images. The following computational parameters were applied: a plane-wave kinetic energy cutoff of 550 eV and a Γ-centered *k*-point mesh of 3 × 2 × 1 for sampling the Brillouin zone for the graphene-succinic acid system, including intermediates and products. Geometric convergence criteria were set to a total energy change of less than 10^{-6} eV and atomic forces below 0.01 eV·Å^{-1}.

The equation used to determine the adsorption energy of succinic acid on graphene(001) surface (GA) is as follows

$$\Delta E_{\text{Comp}} = E_{\text{SA@GA}} - E_{\text{GA}} - E_{\text{SA}} \quad (1)$$

where E_{SA} stands for the total energy of an isolated succinic acid in the gas phase, and $E_{\text{SA@GS}}$ and E_{GA} are the total energies with and without succinic acid molecule adsorption on graphene surface, respectively.

The interfaces were constructed by orienting the graphene(001) surface in contact with two different nickel configurations: one with Ni atoms and oxygen atoms (Gr-Ni) (Fig. S14 in the ESM) and another with only Ni atoms for S_AGr-Ni (Fig. S15 in the ESM). The adsorption of nitrogen intermediates onto both Gr-Ni and S_AGr-Ni (Table S1 in the ESM) was then investigated to compare their potential reactivity toward nitrate reduction.

2.5 *In situ* Raman spectroscopy

In situ Raman spectroscopy was performed using a Teflon cell featuring a quartz window, which was positioned between the sample and the objective lens, as illustrated in Fig. S11 in the ESM. The working electrode was carbon fiber, while Ag/AgCl and Pt wire were used as the reference and counter electrodes, respectively. The electrolyte consisted of 0.1 M $NaNO_3$ in 0.5 M NaOH. A 532 nm laser was used as the excitation source. Prior to measurements, the open-circuit potential (OCP) was recorded, followed by potential-dependent Raman measurements in the range of –0.2 V–−1.0 V vs. RHE. For each applied potential, the system was held under constant electrochemical polarization for 30 min to obtain well-resolved and stable Raman signals.

3 Results and discussion

3.1 Succinic acid assisted exfoliation of graphene

Gr-Ni and S_AGr-Ni were synthesized via ball-milling induced exfoliation of pristine graphite and graphite-succinic-acid mixtures to generate oxygen-functionalized graphene, respectively. Afterwards, the preparation was followed by hydrothermal Ni deposition and high-temperature pyrolysis, where succinic acid derived oxygen functionalities act as anchoring sites that regulate Ni nucleation, suppress aggregation, and stabilize uniformly dispersed Ni nanocluster, as observed in Fig. 1(a). Raman spectroscopy was employed to evaluate the defect density and structural disorder of graphene induced by succinic acid assisted exfoliation. Results revealed that the Gr-Ni retains a sharp G band of ~ 1580 cm^{-1} with a better I_D/I_G ratio of 0.34 than the pristine graphite (Fig. S4 in the ESM), indicating a largely intact sp^2 lattice with limited defect formation (Fig. 1(b)). In contrast, S_AGr-Ni exhibits pronounced G-band broadening and a substantially higher I_D/I_G ratio of 0.98, confirming defect generation and lattice strain induced by oxygen functionalization and exfoliation. This structural disorder directly correlates with N_2 sorption isotherms, as S_AGr-Ni delivers a high Brunauer–Emmett–Teller (BET) surface area of 96 m^2·g^{-1} compared to only 5 m^2·g^{-1} for Gr-Ni, as depicted in Fig. 1(c).

The oxygen enrichment observed in S_AGr-Ni is not incidental but arises from a chemically selective exfoliation pathway driven by succinic acid, which is directly reflected in the C 1s XPS spectra (Figs. 2(a) and 2(b)) derived from the full XPS survey spectra shown in Figs. S5(a) and S5(b) in the ESM. The deconvolution of the C 1s spectra of Gr-Ni (Fig. 2(a)) and S_AGr-Ni (Fig. 2(b)) shows a dominant sp^2 C–C peak at 284.8 eV [29, 30], confirming that the π-conjugated graphene backbone remains largely intact, while additional oxygen-derived components emerge at higher binding energies. Notably, the strong intensities of the C–O (286.6 eV) and C=O (288.1 eV) peaks [31], together with the broader O=C–O signal at 289.1 eV [32] in Fig 2(b), demonstrate substantial enrichment of carboxyl-derived functionalities introduced during succinic-acid-assisted exfoliation.

These experimental observations were further rationalized by density functional theory and *ab initio* molecular dynamics simulations. The simulations reveal, at the atomic level, how succinic acid-derived carboxyl groups preferentially adsorb, dissociate, and electronically interact with graphene to drive oxygen enrichment, exfoliation, and interfacial functionalization. With the calculated DFT and AIMD simulations shown in Figs. S6 and S7 in the ESM, succinic acid preferentially adsorbs in a planar configuration where both carboxyl groups engage the graphene surface, yielding a high adsorption energy of –0.85 eV and a short interfacial distance of 2.70 Å (Figs. 2(c) and 2(d)). In contrast, the T-shaped configuration involving a single interacting carboxyl group (Figs. 2(e) and 2(f)) is significantly less stable (–0.18 eV, 3.12 Å), conclusively identifying –COOH as the thermodynamically preferred exfoliating unit.

Reaction-pathway analysis further reveals that surface-mediated cleavage of succinic acid proceeds most favorably via the –COOH and –CH_2COOH routes, whereas the –OH and –O– pathways exhibit substantially higher energy barriers, as presented in Fig. 2(g). Specifically, after adsorption of succinic acid onto graphene at –0.85 eV, as shown in Fig. 2(c), the calculated activation barriers for intermediate formation are 3.50 eV for –CH_2COOH and 3.56 eV for –COOH, which are significantly lower than those for the –O– (4.04 eV) and –OH (4.53 eV) pathways. Following dissociation, the product-state energies further confirm this trend: –0.58 eV for –O–, 0.17 eV for –OH, 1.02 eV for –CH_2COOH, and 1.33 eV for –COOH fragments.

Various reaction pathways illustrating the dissociation of succinic acid on the graphene surface are also presented in Fig. S8 in the ESM. These results indicate that carboxyl (–COOH)-derived intermediates preferentially govern the exfoliation process and become covalently integrated at the graphene edges, rather than

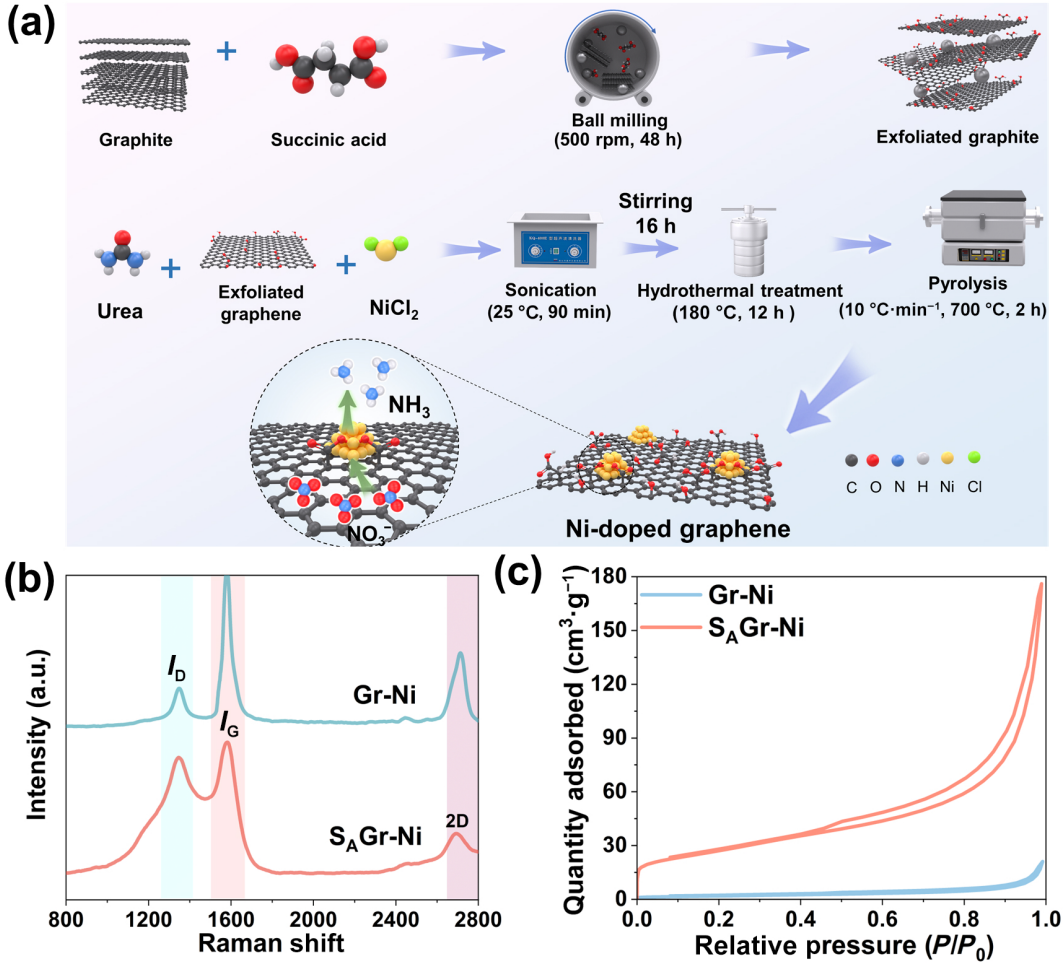

Figure 1 (a) Synthesis procedure of the catalysts Gr-Ni and S_AGr-Ni. (b) Raman spectra and (c) BET analysis of the prepared catalysts.

remaining weakly physisorbed on the surface. This is consistent with the higher XPS intensity of C=O and O–C=O species (Fig. 2(b)), confirming that oxygen functionalities are structurally anchored within the graphene lattice, thereby creating robust anchoring sites for subsequent metal deposition.

3.2 Effective doping Ni nanocluster on exfoliated graphene

Importantly, the carboxyl-rich edge functionalities generated during succinic acid exfoliation suppress graphene restacking and create abundant active sites for Ni anchoring. These sites promote the controlled nucleation and stabilization of highly dispersed Ni nanoclusters, preventing their aggregation into larger metallic particles. This structural property relationship is directly visualized by scanning electron microscopy (SEM), which reveals that Gr-Ni, lacking oxygen anchoring sites, undergoes uncontrolled Ni amalgamation, forming large aggregates of size of 60–80 nn, as observed in Figs. 3(a) and 3(b). In stark contrast, S_AGr-Ni displays a homogeneous distribution of finely confined Ni nanoparticles of 8–10 nm uniformly anchored across exfoliated graphene sheets (Figs. 3(d) and 3(e)). This quantitatively confirms the presence of small and well-exfoliated graphene platelets and the fine Ni nanoparticles, as observed in the SEM images and energy dispersive X-ray spectroscopy (EDS) mappings, which can be observed in Figs. S9 and S10 in the ESM for Gr-Ni and S_AGr-Ni, respectively. Particle size distribution analysis quantitatively corroborates this transition, with Gr-Ni exhibiting a dominant peak at ~ 0.6 μm, indicative of severe aggregation (Fig. 3(c)), whereas S_AGr-Ni shows a narrow size distribution within 0.1–0.4 μm with maxima at ~ 0.11 μm, confirming effective exfoliation and controlled Ni growth (Fig. 3(f)).

High-resolution TEM and high-angle annular dark-field scanning transmission electron microscopy (HAADF-STEM) images clearly reveal the structural differences between the two catalysts. In Gr-Ni (Fig. 3(g)), Ni appears as relatively large and compact nanoparticles with an average size of 60–80 nm, as confirmed by the particle size distribution histogram. These particles are irregularly shaped and partially detached from the graphene surface, indicating limited interfacial contact and a tendency toward aggregation. The weak interaction between Ni and pristine graphene results in reduced dispersion and fewer accessible interfacial active sites.

In contrast, S_AGr-Ni (Fig. 3(h)) exhibits uniformly distributed Ni nanoclusters with a significantly smaller average size of 8–10 nm. The histogram confirms the narrow particle size distribution, indicating controlled nucleation. Notably, the nanoclusters are preferentially anchored along the graphene edges and oxygen-enriched regions (highlighted in the image), suggesting strong metal–support interaction. This intimate coupling maximizes exposed active surface area and interfacial contact.

The differences in structural development become more

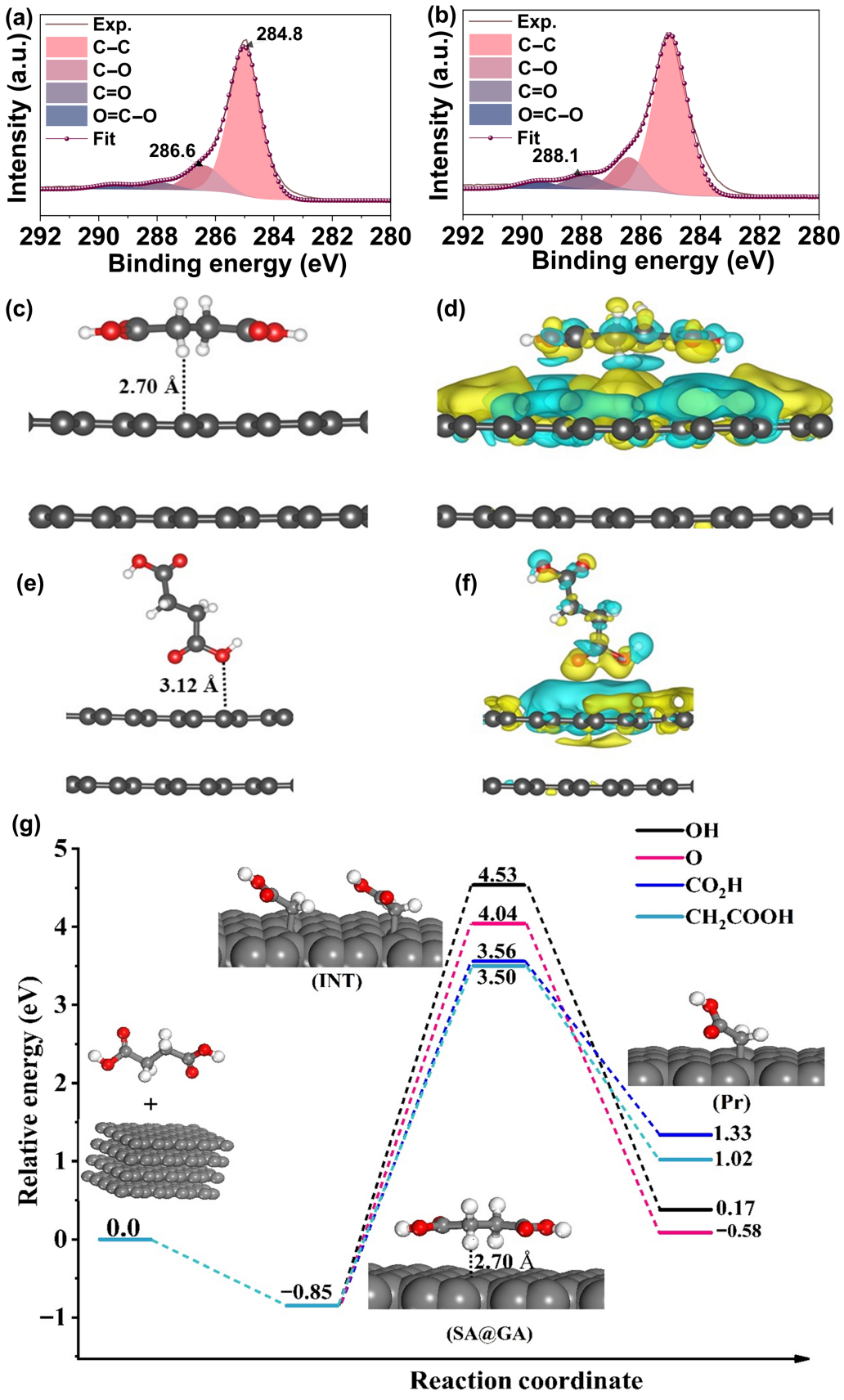

Figure 2 ((a) and (b)) Deconvoluted C 1s XPS spectra for (a) Gr-Ni and (b) S_AGr-Ni. ((c) and (e)) Succinic acid interacting with a graphene layer in (c) planar configuration and (e) T-shaped configuration, and ((d) and (f)) the corresponding three-dimensional charge density difference for each SA/graphene interface. (g) Computed reaction mechanism and energy landscape for succinic acid dissociation on graphene, illustrating a key step in the exfoliation process.

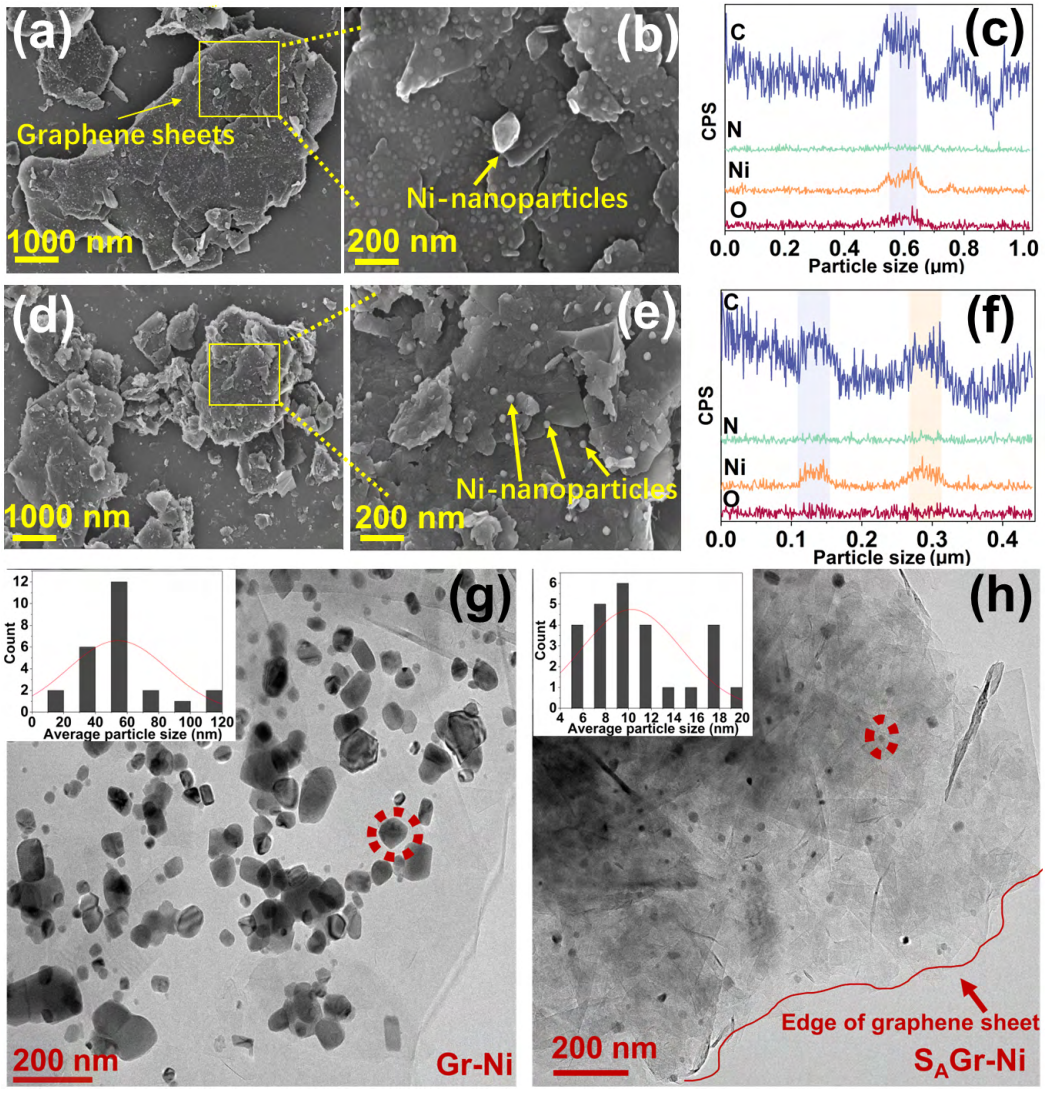

Figure 3 ((a) and (b)) SEM images of Gr-Ni and (c) corresponding analysis of particle size versus CPS of Gr-Ni. ((d) and (e)) SEM images of S_AGr-Ni and (f) corresponding analysis of particle size versus CPS of S_AGr-Ni. ((g) and (h)) TEM images of (g) Gr-Ni along with an inset of calculated average particle size and (h) S_AGr-Ni along with an inset of calculated average particle size at 200 nm resolution.

pronounced in the HR-TEM and corresponding fast Fourier transform (FFT) analyses in Fig. 4, which reveal fundamentally distinct Ni growth behaviors in the two systems. In Gr-Ni, large and irregular particles dominate, where lattice fringes of 0.203 nm (Fig. 4(a)) correspond to Ni(111) [33], yet surface discontinuities and additional fringes of 0.240 nm [34] assigned to NiO(211) [35] indicate partial oxidation (Fig. 4(b)). The broadened and diffuse FFT features further reflect mixed crystalline domains and structural disorder. This structural heterogeneity is further corroborated by HAADF imaging of Gr-Ni (Figs. 4(e)–4(h)), where the spatial distribution of Ni (Fig. 4(f)) and O (Fig. 4(h)) does not fully overlap, indicating non-uniform interfacial interaction and localized oxidation.

In Gr-Ni, the deconvolution of O 1s spectra is dominated by a pronounced peak centered at ~ 531 eV (Fig. 4(m)), which is characteristic of lattice oxygen associated with Ni–O bonds (NiO_x/$Ni(OH)_2$ species). This observation confirms that a substantial fraction of surface Ni is present in oxidized form, consistent with the Ni^{2+} dominated Ni 2p spectrum, as depicted in Fig. 4(o). Additional peaks at higher binding energies from ~ 531 to 534 eV, typically attributed to C=O and C–OH, respectively, are comparatively limited, reflecting the low density of intrinsic oxygen functionalities on bare graphene (Fig. 4(m)). The predominance of the Ni–O component in the O 1s spectrum therefore indicates that oxygen is mainly involved in Ni oxidation rather than interfacial Ni–O–C coordination. This supports the scenario in which, due to insufficient anchoring groups, Ni species undergo surface oxidation and aggregate into larger NiO-rich particles, as observed in HR-TEM images.

However, S_AGr-Ni forms uniformly dispersed nanoclusters with continuous *d*-spacing of 0.200 nm Ni(311) lattice fringes (Fig. 4(c)) and no detectable NiO-related spacing. The FFT patterns presented in Fig. 4(d) exhibit sharp and symmetric spots that index to the Ni(311) crystallographic plane. This confirms that the catalytically active phase is the metallic Ni layer. In contrast, for Gr-Ni, the NiO layer was identified as the active layer for NO_3^- reduction (Fig. 4(b)). This structural information serves as a reliable input for constructing DFT models to predict the mechanism of NO_3^- reduction to NH_3. The elemental maps in Figs. 4(j) (Ni) and 4(l) (O) for S_AGr-Ni show that O is distributed over a broader area,

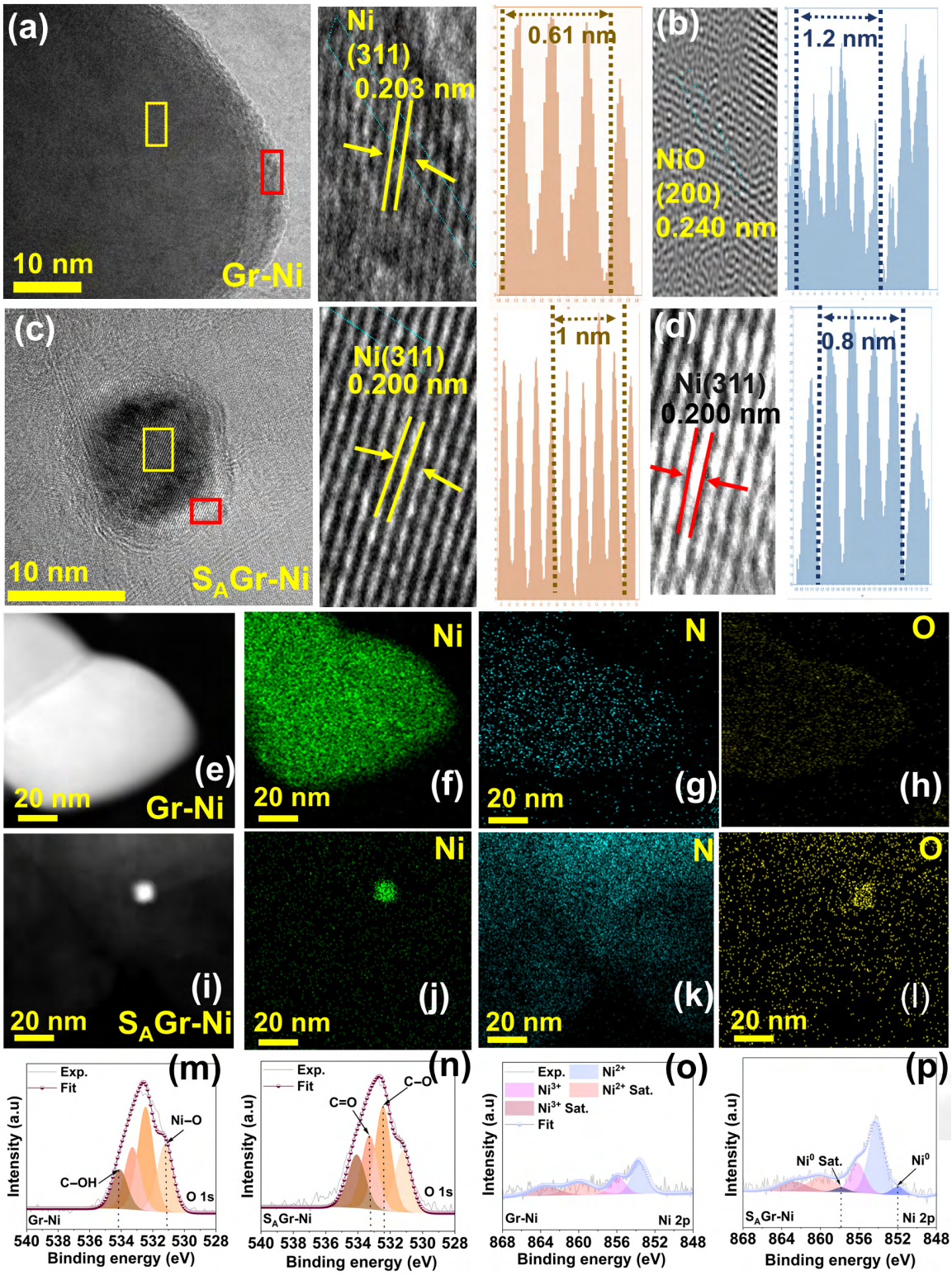

Figure 4 (a) High resolution TEM image of Gr-Ni and its FFT patters. (b) FFT patters of Gr-Ni outer layer. (c) TEM image of S_AGr-Ni and its FFT patterns. (d) FFT patters of S_AGr-Ni outer layer. (e) HAADF image of Gr-Ni and ((f)–(h)) corresponding EDS mappings. (i) HAADF image of S_AGr-Ni and ((j)–(l)) corresponding EDS mappings. ((m) and (n)) Deconvoluted O 1s XPS spectra of (m) Gr-Ni and (n) S_AGR-Ni. ((o) and (p)) Deconvoluted Ni 2p XPS spectra of (o) Gr-Ni and (p) S_AGr-Ni.

while Ni is confined within these O-rich domains. This suggests that oxygen functionalities encapsulate and stabilize the Ni nanoclusters, restricting particle aggregation. Correspondingly, XPS spectra (Fig. 4(n)) reveals intensified C=O (~ 533.1 eV) and C–O (~ 532.2 eV) peaks in O 1s, together with a stronger metallic Ni^0 peak at ~ 852.0 eV (Fig. 4(p)) [36] and attenuated satellite features at 857.8 eV, indicating enhanced electronic screening and suppressed bulk oxidation.

Collectively, the sharper and higher-intensity FFT reflections, enriched oxygen-functional group signals, and strengthened Ni^0

XPS peaks demonstrate that oxygen-functionalized graphene promotes the formation of highly crystalline, electronically stabilized Ni nanoclusters while preventing extensive NiO formation.

3.3 Electrochemical nitrate reduction with S_AGr-Ni

To evaluate and compare the electrocatalytic NO_3^- reduction performance, both Ni-based graphene catalysts were tested using a standard three-electrode configuration in a divided H-type electrochemical cell. The electrocatalytic behavior of the catalysts was first evaluated by LSV in 1 M NaOH with and without NO_3^- at potential between 1.2 and −1.2 V vs. RHE, as represented in Fig. 5(a). Bare carbon paper shows negligible current response, confirming its electrochemical inertness. Notably, both Gr-Ni and S_AGr-Ni exhibited substantially higher current densities in NO_3^- containing electrolytes than in NO_3^- free solutions. This NO_3^- dependent current enhancement confirms the intrinsic NO_3^-RR activity of the catalysts [37] and their effective suppression of parasitic HER under the applied potentials [38, 39]. Particularly, S_AGr-Ni delivers substantially higher current densities across the entire cathodic window, reaching −55–−58 mA·cm^{-2} at −1.0 V vs. RHE, surpassing Gr-Ni (~ −47 mA·cm^{-2}), indicative of accelerated nitrate reduction kinetics.

Chronoamperometric (*i* vs. *t*) measurements coupled with quantitative product analysis provide direct evidence of the catalytic activity. S_AGr-Ni achieves a peak NH_3 production rate of 12.9 mg·h^{-1}·cm^{-2}, as shown in Fig. 5(b), with a Faradaic efficiency of 90% (Fig 5(c)) at a potential of −1.2 V vs. RHE, representing an enhancement of 70% in yield and an increase of 12% in FE compared to Gr-Ni under identical conditions. The stable current profiles over 90 min further confirm sustained catalytic operation without noticeable deactivation.

Electrochemical impedance spectroscopy (EIS) further corroborates this trend, where S_AGr-Ni exhibits a markedly smaller semicircle diameter than Gr-Ni (Fig. 5(d)), reflecting lower charge-transfer resistance (R_{ct}) and reflecting faster interfacial electron–proton kinetics [40] enabled by the oxygen-rich graphene-Ni nanocluster. These findings are further supported by CV measurements. Compared to Gr-Ni (Fig. 5(e)), S_AGr-Ni (Fig. 5(f)) exhibits a markedly higher capacitive current and more pronounced cathodic features in the negative potential region from −0.6 to −0.9 V vs. RHE, indicative of an increased density of adsorbed hydrogen intermediates (H*). These broadened H adsorption/desorption responses suggest a wider distribution of stabilized H* species on S_AGr-Ni. In contrast, Gr-Ni displays weaker and less distinct H* features, consistent with hydrogen adsorption which might be occurring predominantly irregular Ni surfaces. Whereas, the enhanced H* reservoir on S_AGr-Ni facilitates proton-coupled electron transfer to adsorbed NO_3^-/NO_x intermediates, leading to higher NH_3 yield and Faradaic efficiency [36].

Furthermore, TBA scavenger experiments corroborate the involvement of hydrogen-related intermediates in the nitrate

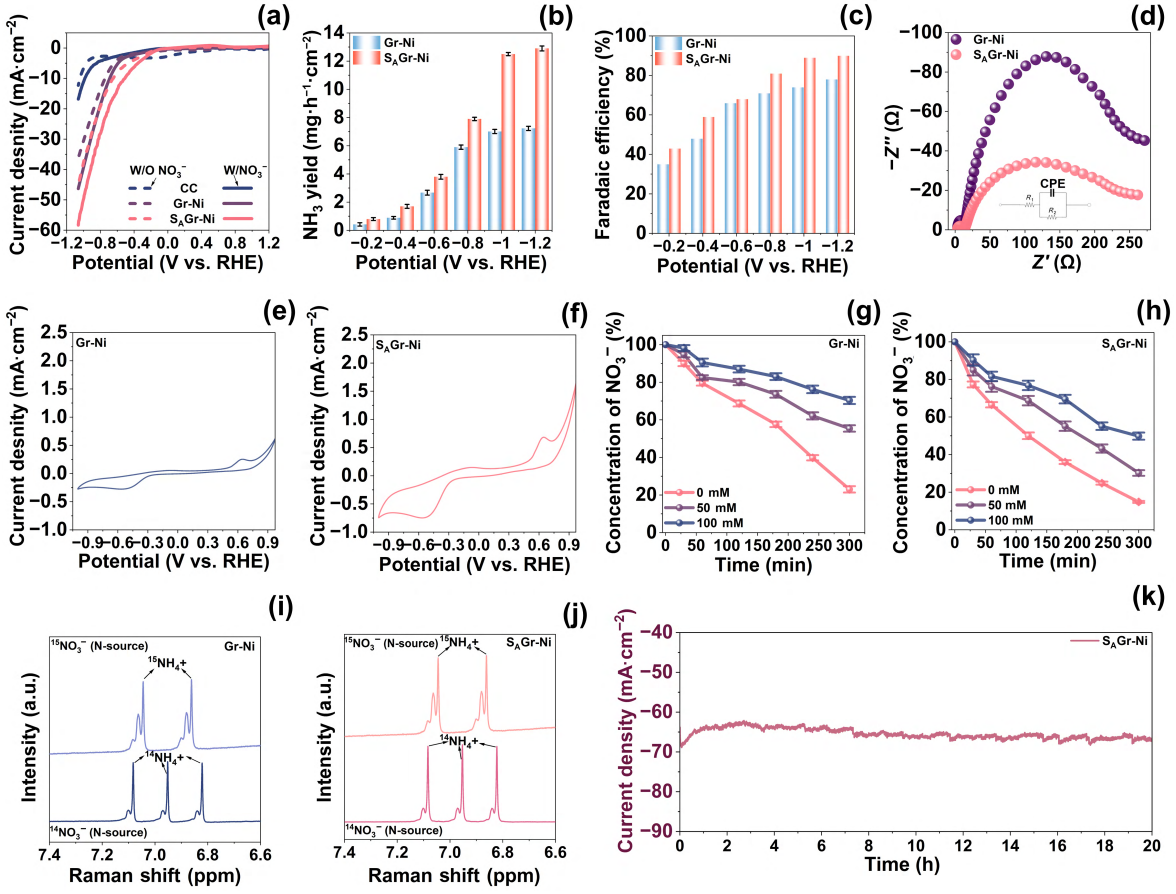

Figure 5 (a) LSV curve of the bare carbon paper, Gr-Ni, and S_AGr-Ni. (b) NH_3 yield rate, (c) Faradaic efficiency, and (d) EIS plots of Gr-Ni and S_AGr-Ni. ((e) and (f)) CV measurements of (e) Gr-Ni and (f) S_AGr-Ni. ((g) and (h)) TBA quenching experiments for (g) Gr-Ni and (h) S_AGr-Ni. ((i) and (j)) ^{1}H NMR spectra of the electrolyte after the electrocatalytic nitrate reduction reaction using $^{15}NO_3^-$ and $^{14}NO_3^-$ as the nitrogen source for (i) Gr-Ni and (j) S_AGr-Ni. (k) Long-term stability testing of S_AGr-Ni in a flow cell configuration.

reduction mechanism. Upon the addition of TBA, the NH_3 yield evaluated at −1.0 V vs. RHE over 300 min in 200 mg·L^{-1} NO_3^- decreases sharply for Gr-Ni (Fig. 5(g)), indicating that its nitrate reduction activity predominantly depends on weakly adsorbed surface hydrogen intermediates (H*), which are readily scavenged by TBA. In contrast, S_AGr-Ni retains substantially higher activity under identical conditions (Fig. 5(h)), demonstrating a reduced sensitivity to H* quenching. This behavior indicates that S_AGr-Ni stabilizes hydrogen species more effectively through Ni nanocluster formation which might provide alternative proton reservoirs beyond transient surface radicals.

Isotopic labeling experiments performed provided the clear evidence for the origin of NH_3. The ^{1}H NMR spectra exhibit distinct doublets at 6.90 ppm for Gr-Ni (Fig. 5(i)) and at 7.07 ppm for S_AGr-Ni (Fig. 5(j)), characteristic of $^{15}NH_4^+$ formed through ^{1}H–^{15}N coupling. This unequivocally confirms that ammonia is generated from NO_3^- reduction. For comparison, the ^{1}H NMR spectrum of the control sample $^{14}NO_3^-$ shows a characteristic triplet between 6.8 and 7.1 ppm, consistent with $^{14}NH_4^+$. The distinct difference between the doublet and triplet patterns further supports the successful isotopic labeling and the exclusive origin of NH_3 from NO_3^- reduction. Moreover, no ammonia signal was observed in the absence of nitrate (Fig. S11(c) in the ESM), effectively ruling out any contribution either from contamination or catalyst-derived nitrogen. The ammonia yield of S_AGr-Ni quantified by NMR by using the standard curve shown in Fig. S11(a) in the ESM is 10.8 mg·h^{-1}·cm^{-2}, which agrees well with the ultraviolet–visible (UV–vis) value of 12.9 mg·h^{-1}·cm^{-2}, as depicted in Fig. S11(d) in the ESM. The Faradaic efficiency obtained from NMR is about 80%, slightly lower than the 90% measured by UV–vis, but both methods show consistent trends for the catalyst S_AGr-Ni.

Additionally, under continuous flow operation at a constant applied potential of −1.2 V vs. RHE in 1 M NaOH and 0.1 M $NaNO_3$, the S_AGr-Ni catalyst maintained a stable current density over 20 h, as depicted in Fig. 5(k). The current density initially stabilized at 68.9 mA·cm^{-2} within the first hour and then remained nearly constant between −62 and −68 mA·cm^{-2} for the remaining duration. Importantly, the final current density at 20 h is approximately −67.4 mA·cm^{-2}, which is 97.8% of the current density at 1 h of −68.9 mA·cm^{-2}, indicating negligible decay during extended operation and confirming that the catalyst is intrinsically robust under practical reaction conditions.

3.4 Selectivity and stability of S_AGr-Ni for electrochemical ammonia generation

The time-dependent NO_3^- reduction profiles provide direct kinetic evidence of the distinct reaction pathways on the two catalysts. For Gr-Ni (Fig. 6(a)), NO_3^- concentration gradually decreases from 100% to 25% over 300 min; however, a significant accumulation of NO_2^- is observed, reaching 29.2% at the end of electrolysis. Concurrently, NH_3 formation increases slowly and reaches only 50.2%, while 20.6% of nitrogen remains distributed in other byproducts, as shown in the pie chart in Fig. 6(b). The pronounced NO_2^- buildup indicates that the hydrogenation of $*NO_2$ and subsequent intermediates is kinetically limited, interrupting the multi-electron transfer cascade and lowering overall NH_3 selectivity. In contrast, S_AGr-Ni exhibits a markedly different behavior. NO_3^- is rapidly consumed to below 15% within 300 min (Fig. 6(c)), while NO_2^- remains at a minimal level of 7.8% throughout the reaction. NH_3 production increases steadily to 85.6%, with only 6.6% assigned to other nitrogen species, as depicted in Fig. 6(d). This suppressed nitrite accumulation demonstrates a continuous and efficient hydrogenation sequence from NO_3^- to NH_3 without intermediate stagnation.

The selectivity trend as a function of applied potential further supports this observation, which is evident in Fig. 6(e). At a potential of −1.2 V vs. RHE, S_AGr-Ni achieves an NH_3 selectivity of 78%, significantly higher than the 48% obtained for Gr-Ni under identical conditions. Moreover, the NH_3 yield rate remains stable at 12–13 mg·h^{-1}·cm^{-2} with a Faradaic efficiency close to 85%–90% over 20 consecutive cycles (Fig. 6(f)), confirming both kinetic superiority and operational durability.

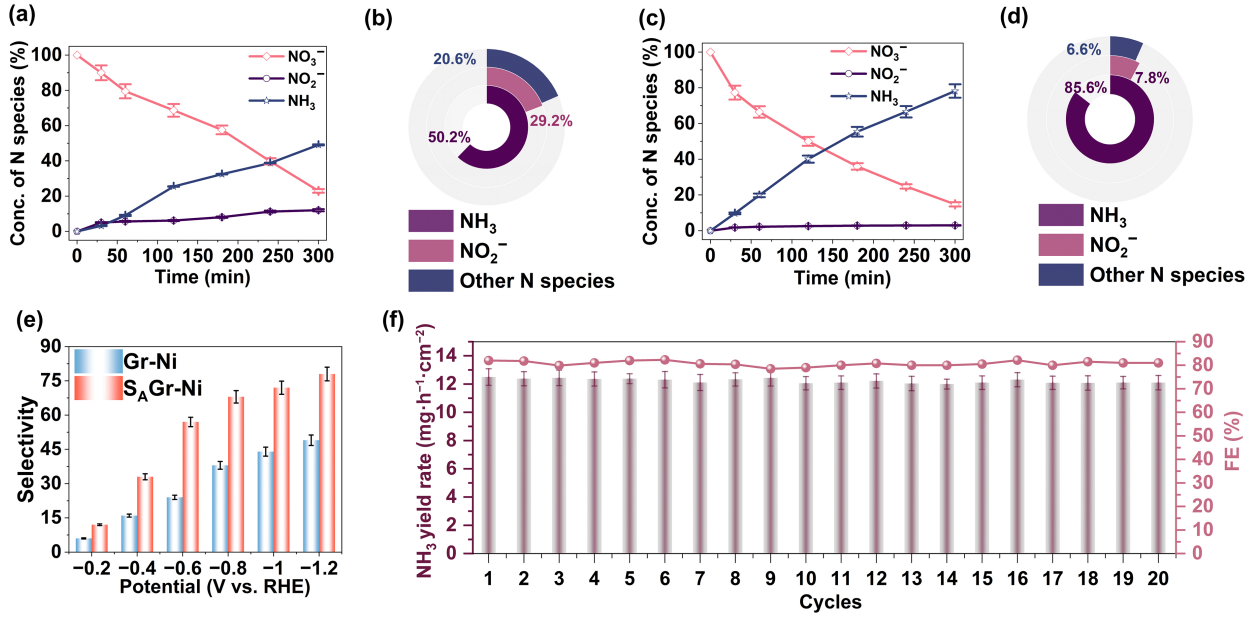

Figure 6 ((a)–(d)) Time-dependent evolution of nitrogen-containing species during electrochemical nitrate reduction on (a) Gr-Ni and (b) the corresponding product distribution summarized as a pie chart, and on (c) S_AGr-Ni with (d) its corresponding pie chart. (e) Selectivity toward NH_3 formation for the two catalysts. (f) Cycling stability of S_AGr-Ni during repeated nitrate reduction tests.

3.5 Structural evolution and mechanistic investigation

To elucidate the structural reconstruction and identify the active phase of S_AGr-Ni during nitrate reduction, the Ni oxidation state was examined by high-resolution XPS. After NO_3^- reduction reaction at −0.4 V vs. RHE, the deconvoluted Ni 2p spectrum of S_AGr-Ni shows a pronounced increase in the metallic Ni^0 peak at 851.9 eV, accompanied by a characteristic satellite feature at 857.9 eV, as shown in Fig. 7(a). In contrast, the relative contributions of oxidized Ni^{2+} and Ni^{3+} species are significantly decreased compared to those in the fresh S_AGr-Ni sample (Fig. 4(p)), indicating that the catalyst surface undergoes reduction under cathodic potentials. This transformation suggests the formation of an electron-rich Ni^0 phase during operation. This observation is further corroborated by *in situ* Raman spectroscopy, as shown in Fig. 7(b). At open-circuit potential (OCP), the Raman spectrum reveals a characteristic peak at 450 cm^{-1} corresponding to the $Ni(OH)_2$ phase [41] of S_AGr-Ni. Upon application of cathodic potentials, this peak gradually diminishes, suggesting conversion to a reduced nickel phase that is not Raman-active. To identify reaction intermediates for subsequent DFT analysis, we first observed a bending mode of the $-NO_2$ group at 790 cm^{-1} [39], followed by stretching vibrations of NO_3^- at 1047 $cm{\cdot}cm^{-1}$ and adsorbed NO_3^- ($_aNO_3^-$) at 1087 $cm{\cdot}cm^{-1}$ [42]. The reduction of NO_3^- to NO_2^- occurs at cathodic potentials of −0.2 V vs. RHE. Afterwards, asymmetric vibrations characteristic of the $-NH_2$ emerges at 1180 cm^{-1} [43] (−0.4 V vs. RHE). The emergence of −NH moieties after NO_2^- formation suggests a sequential reduction

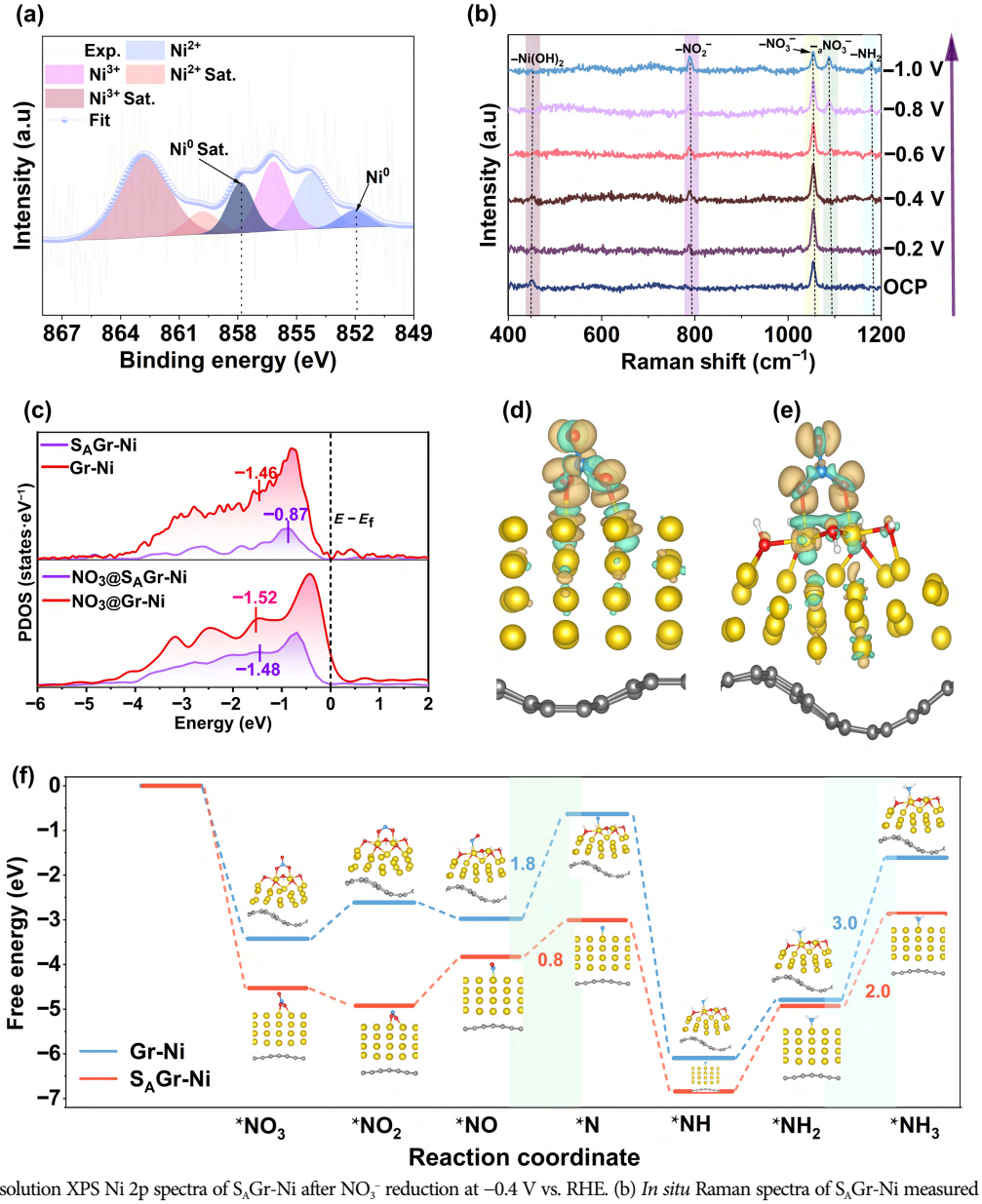

Figure 7 (a) High-resolution XPS Ni 2p spectra of S_AGr-Ni after NO_3^- reduction at −0.4 V vs. RHE. (b) *In situ* Raman spectra of S_AGr-Ni measured at OCP and various cathodic potentials (vs. RHE) during NO_3^- reduction. (c) PDOS sates of S_AGr-Ni and Gr-Ni before and after NO_3^- adsorption, and d-band center values have provided in eV. ((d) and (e)) Charge density distribution of (d) S_AGr-Ni and (e) Gr-Ni. (f) Calculated free-energy diagrams for the NO_3^- reduction reaction on Gr-Ni and S_AGr-Ni, illustrating the relative Gibbs free energies of the adsorbed intermediates along the reaction pathway. The insets show the optimized structural models for both catalysts with representative adsorbed configurations. In the atomic models, carbon atoms (graphene) are depicted in black, Ni atoms in gold, oxygen atoms in red, hydrogen atoms in white, and nitrogen atoms in blue.

pathway in which NO_3^- is first converted to NO_2^-, followed by stepwise hydrogenation to NH_3. Additionally, the D and G bands of SAGr-Ni are observed at 1351 and 1610 cm^{-1}, respectively, at OCP (Fig. S12 in the ESM). However at −1.0 V vs. RHE, the attenuation of the D band indicates a decrease in defect-related disorder, which may arise either from surface reconstruction or intermediate adsorption during NO_3^- reduction [44]. Collectively, these spectroscopic findings identify the reduced nickel phase, most reasonably metallic Ni^0 as the active site for nitrate reduction, thereby providing a critical experimental foundation for constructing realistic DFT simulation models.

DFT calculations provide further mechanistic insight into the superior NH_3 production activity of S_AGr-Ni. The projected density of states (PDOS) shown in Fig. 7(c) reveals that the Ni 3d d-band center for S_AGr Ni is located at −0.87 eV, which is upshifted by 0.59 eV relative to that of Gr-Ni (−1.46 eV). This upshift indicates a stronger electronic interaction between the Ni active sites and NO_3^-, thereby facilitating its adsorption and activation [45]. Upon NO_3^- adsorption, the d-band centers of both systems shift toward the Fermi level, reaching −1.48 eV for S_AGr-Ni and −1.52 eV for Gr-Ni. This positive shift reflects significant electronic coupling between the adsorbate and the Ni active sites.

Charge density distribution maps additionally clarify this by revealing more intensified and spatially confined electron localization lobes around Ni in S_AGr-Ni (Fig. 7(d)), indicating stronger directional orbital hybridization between Ni and NO_3^- compared to Gr-Ni (Fig. 7(e)). Consequently, this finding is consistent with the electronic structure characteristics revealed by the DFT-simulated models (Table S1 in the ESM). Based on the optimized structures, the reaction pathway involves the adsorption of NO_3^-, successive deoxygenation steps ($*NO_3 \rightarrow *NO_2 \rightarrow *NO \rightarrow *N$), followed by stepwise hydrogenation ($*N \rightarrow *NH \rightarrow * NH_2 \rightarrow *NH_3$), and finally NH_3 desorption (Fig. 7(f)). Structural models of Gr-Ni (Fig. S14 in the ESM) and S_AGr-Ni (Fig. S15 in the ESM) with all elementary intermediates adsorbed were constructed, and the free energies of each proton–electron transfer step were calculated. Both catalysts exhibit the highest uphill barrier at the $*NO \rightarrow *N$ step, identifying it as the rate-determining step, as shown in the first highlighted region of Fig. 7(f). For Gr-Ni, this step requires an energy input of 1.8 eV, indicating sluggish N–O bond cleavage and a strong tendency toward incomplete reduction. In contrast, S_AGr-Ni shows a significantly reduced barrier of 0.8 eV, lowered by approximately 1.0 eV, demonstrating facilitated deoxygenation kinetics.

Furthermore, the elementary step from $*NO_3$ to NO_2 displays fundamentally different thermodynamic behavior on the two catalysts. On S_AGr-Ni, this step proceeds downhill in free energy, indicating spontaneous nitrate activation. In contrast, on Gr-Ni the same transformation remains uphill, reflecting insufficient activation of surface-bound nitrate. The downhill character on S_AGr-Ni prevents intermediate accumulation and enables continuous reduction, whereas the uphill barrier on Gr-Ni favors partial reduction and nitrite release, thereby limiting ammonia selectivity [46, 47]. The more balanced energetics across subsequent hydrogenation steps ($*N \rightarrow *NH \rightarrow *NH_2 \rightarrow *NH_3$) on S_AGr-Ni avoid excessive stabilization of intermediates, enabling a continuous multi-electron transfer cascade toward NH_3 formation. The reduced RDS barrier and optimized intermediate stabilization on S_AGr-Ni provide strong theoretical evidence for its superior NH_3 selectivity, consistent with the experimentally observed 78% at −1.2 V vs. RHE compared to 48% for Gr-Ni. Collectively, these observations establish S_AGr-Ni as a superior catalyst for ammonia production and selectivity compared to the other catalysts evaluated, as summarized in Table S2 in the ESM.

4 Conclusions

In summary, we demonstrated that succinic-acid functionalization fundamentally transforms graphene from an inert support into an oxygen-enriched and catalytically active support that governs Ni nucleation, electronic structure, and reaction selectivity for electrochemical nitrate reduction. Carboxyl-derived oxygen groups preferentially anchor Ni nanoclsuter of size of 8–10 nm as DFT/AIMD simulations identifying intact –COOH groups as the dominant exfoliating and coordinating units. Interfacial oxygen enrichment stabilizes partially oxidized Ni^0/Ni^{2+} sites and suppresses graphene restacking, yielding a high surface area of 96 $m^2 \cdot g^{-1}$. The nanocluster Ni interface in S_AGr-Ni optimizes hydrogen adsorption and sustains H* availability, as evidenced by enhanced H adsorption features in CVs, reduced charge-transfer resistance, and mitigated NH_3 activity loss upon TBA addition. Consequently, S_AGr-Ni delivers a high NH_3 yield rate of 12.9 $mg \cdot h^{-1} \cdot cm^{-2}$ with a Faradaic efficiency of ~ 90% at −1.2 V vs RHE, outperforming Gr-Ni by ~ 70% in yield and ~ 12% in FE. Kinetic and selectivity studies further reveal rapid NO_3^- conversion with minimal NO_2^- accumulation and stable performance over repeated cycles, highlighting the decisive role of carboxyl-mediated exfoliation resulted in formation of Ni cluster coupling in steering proton-coupled electron transfer toward selective ammonia formation. This study establishes oxygen-engineered graphene-Ni nanocluster as a powerful design principle for high-rate and selective nitrate-to-ammonia electrocatalysis.

Electronic Supplementary Material: Supplementary material (chemicals and reagents, instrument calibration curves, Raman and XPS spectra, DFT-optimized structures, NMR spectra, and a comparison table of the catalytic performance with previously reported catalysts) is available in the online version of this article at https://doi.org/10.26599/NR.2026.94908824.

Data availability

All data needed to support the conclusions in the paper are presented in the manuscript and the Electronic Supplementary Material. Additional data related to this paper may be requested from the corresponding author upon request.

Acknowledgements

This study was supported by the National Natural Science Foundation of China (No. 52370169), China Postdoctoral Science Foundation (No. 2023M742247), the Fundamental Research Funds for the Central Universities of Huaqiao University (No. ZQN-913), and the research fund from Huaqiao University (No. 23BS122). The authors also thanks to the TEM analysis offered by Analytical and Testing Center of Huaqiao University.

Declaration of competing interest

All the contributing authors report no conflict of interests in this work.

Author contribution statement

N. G. performed the experimental work, analyzed the data, and wrote the manuscript. Z. L. Z. and W. J. L. assisted with the procurement of materials. F. L. provided critical suggestions to the manuscript. S. B. conducted all DFT calculations and simulation studies. Y.-b. H. conceived the research idea, supervised the project, provided critical guidance on the manuscript, and provided financial support too. All the authors have approved the final manuscript.

Use of AI statement

None.

References

[1] Alencar, L. M.; Silva, A. W. B. N.; Trindade, M. A. G.; Salvatierra, R. V.; Martins, C. A.; Souza, V. H. R. One-step synthesis of crumpled graphene fully decorated by copper-based nanoparticles: Application in H_2O_2 sensing. *Sens. Actuators B: Chem.* **2022**, *360*, 131649.

[2] Bonaccorso, F.; Colombo, L.; Yu, G. H.; Stoller, M.; Tozzini, V.; Ferrari, A. C.; Ruoff, R. S.; Pellegrini, V. Graphene, related two-dimensional crystals, and hybrid systems for energy conversion and storage. *Science* **2015**, *347*, 1246501.

[3] Gu, J. X.; Shi, Z. X.; Yan, T. R.; Tian, M.; Chen, Z. A.; Chen, S. Q.; Ding, Y. F.; Lu, M. Y.; Zou, Y. H.; Zhang, J. C. et al. Graphene chainmail-enabled moderate precatalyst phase evolution for sustainable polysulfide electrocatalysis in Li-S batteries. *Small* **2025**, *21*, 2407196.

[4] Zhang, P. X.; Wang, Q.; Zhang, Y. X.; Lin, M.; Zhou, X.; David, A.; Ustyuzhanin, A.; Chen, M. S.; Katsnelson, M. I.; Trubyanov, M. et al. Strain-induced crumpling of graphene oxide lamellas to achieve fast and selective transport of H_2 and CO_2. *Nat. Nanotechnol.* **2025**, *20*, 1254–1261.

[5] Sun, M. Y.; Wang, S.; Liang, Y. B.; Wang, C.; Zhang, Y. H.; Liu, H.; Zhang, Y.; Han, L. Flexible graphene field-effect transistors and their application in flexible biomedical sensing. *Nano-Micro Lett.* **2025**, *17*, 34.

[6] El-Khair, M. A. A.; Abo El Naga, A. O.; Elwakeel, K. Z.; Elgarahy, A. M.; Priya, A. K.; Yadav, K. K.; Morshedy, A. S. The promise of graphene-based photocatalytic materials for wastewater remediation: A scoping review. *Coord. Chem. Rev.* **2025**, *544*, 216961.

[7] Jeon, I. Y.; Bae, S. Y.; Seo, J. M.; Baek, J. B. Scalable production of edge-functionalized graphene nanoplatelets via mechanochemical ball-milling. *Adv. Funct. Mater.* **2015**, *25*, 6961–6975.

[8] Kang, X. F.; Fu, W. Y.; Schneider, G. F. Experimental strategies to fabricate mechanically exfoliated graphene sub-nanofluidic devices. *Carbon* **2025**, *234*, 120005.

[9] Wang, H. F.; Tang, C.; Zhang, Q. A review of graphene-based 3D van der Waals hybrids and their energy applications. *Nano Today* **2019**, *25*, 27–37.

[10] Liu, Z. Y.; Huang, X. H.; Liu, X.; Liu, J.; Wang, M. T.; Ding, T.; Yan, L. H.; Zhang, Z. H.; Shi, G. S. Electrochemical synthesis of metasequoia-like reduced graphene oxide coated cobalt-silver catalyst for stable and efficient electrocatalytic nitrate reduction to ammonia. *Small* **2025**, *21*, 2408566.

[11] Hu, Q.; Shang, C. Y.; Chen, X. B.; Qi, S.; Huo, Q. H.; Yang, H. P.; He, C. X. Subnanometric nickel phosphide heteroclusters with highly active $Ni^{\delta+}$–$P^{\delta-}$ pairs for nitrate reduction toward ammonia. *J. Am. Chem. Soc.* **2025**, *147*, 12228–12238.

[12] Yuan, H. F.; Hong, M.; Huang, X. Z.; Qiu, W. T.; Dong, F.; Zhou, Y.; Chen, Y. P.; Gao, J. Q.; Yang, S. H. Graphene chainmail shelled dilute Ni-Cu alloy for selective and robust aqueous phase catalytic hydrogenation. *Adv. Sci.* **2024**, *11*, 2304349.

[13] Jeon, I. Y.; Choi, H. J.; Jung, S. M.; Seo, J. M.; Kim, M. J.; Dai, L. M.; Baek, J. B. Large-scale production of edge-selectively functionalized graphene nanoplatelets via ball milling and their use as metal-free electrocatalysts for oxygen reduction reaction. *J. Am. Chem. Soc.* **2013**, *135*, 1386–1393.

[14] Zhu, H. H.; Cao, Y. L.; Zhang, J. Z.; Zhang, W. L.; Xu, Y. H.; Guo, J. X.; Yang, W. R.; Liu, J. Q. One-step preparation of graphene nanosheets via ball milling of graphite and the application in lithium-ion batteries. *J. Mater. Sci.* **2016**, *51*, 3675–3683.

[15] Teng, X. Y.; Yan, M. Q.; Bi, H. Spectra investigation on surface characteristics of graphene oxide nanosheets treated with tartaric, malic and oxalic acids. *Spectrochim. Acta Part A: Mol. Biomol. Spectrosc.* **2014**, *118*, 1020–1024.

[16] Hong, J. B.; Fan, S. H.; Wu, Y. L.; Wang, C. X.; Li, Z. F.; Chen, J.; Zhong, S. W. Xylitol-assisted ball milling of graphite to prepare long-cycle and high-capacity graphene nanosheet as lithium-ion anode materials. *J. Mater. Sci.* **2021**, *56*, 18200–18209.

[17] Lee, J. G.; Oh, K. H.; Kang, S. W.; Yang, J. I.; Seo, W. S.; Park, J. C. Efficient mechanochemical synthesis of high-performance NiPd alloy nanoparticle catalysts on graphene. *Appl. Surf. Sci.* **2025**, *695*, 162936.

[18] Yu, Z. H.; Yang, W. S.; Zhou, C.; Zhang, N. B.; Chao, Z. L.; Liu, H.; Cao, Y. F.; Sun, Y.; Shao, P. Z.; Wu, G. H. Effect of ball milling time on graphene nanosheets reinforced Al6063 composite fabricated by pressure infiltration method. *Carbon* **2019**, *141*, 25–39.

[19] Acevedo-Guzmán, D. A.; Monroy-Torres, B.; Rudolf, P.; Basiuk, V. A.; Basiuk, E. V. Green mechanochemical fabrication of graphite-lanthanide oxide nanocomposites. *RSC Mechanochem.* **2025**, *2*, 443–458.

[20] Jayant, V.; Kumar, R.; Tyagi, P.; Yusuf, M. Grinding and milling (mechanochemical) methods: An excellent greener approach to develop sustainable materials. In *Green Chemistry*. Prasad, L.; Khan, S. A.; Jain, A. K.; Varma, R. S., Eds.; Elsevier: Amsterdam, 2025; pp 133–168.

[21] Atalie, D.; Abtew, M. A.; Zhao, L. Recent advances in bio-based nonwoven materials: Sustainable production, applications, and circular economy. *J. Nat. Fibers* **2025**, *22*, 2565661.

[22] Zhang, R.; Chen, Z. L.; Li, Y.; Chen, D. L.; Wang, T.; Wang, B. R.; Zhou, Q. L.; Cheng, S. W.; Xu, D.; Wang, X. H. et al. Enhanced photodynamic therapy efficacy of Ni-doped/oxygen vacancy double-defect Ni-ZnO@C photosensitizer in bacteria-infected wounds based on ROS damage and ATP synthesis inhibition. *J. Mater. Sci. Technol.* **2024**, *192*, 173–189.

[23] Wan, K. C.; Luo, C. Q.; Wang, J.; Xu, W.; Pei, X. J.; Yang, D. J.; Ming, P. W.; Zhang, C. M.; Li, B. Rational design of platinum-based confined electrocatalysts for oxygen reduction reaction. *Carbon Neutralizat.* **2025**, *4*, e70062.

[24] Zhuang, L.; Wen, Z. H.; Liu, Y. W.; Yang, J.; Yu, H. L.; Chu, Y. H. Unveiling the oxidation mechanisms of high-entropy carbides through atomic-scale dynamic observation. *Adv. Mater.* **2025**, *37*, 2417846.

[25] Velmurugan, S.; Anupriya, J.; Chen, S. M.; Traiwatcharanon, P.; Cheng, S. H.; Wongchoosuk, C. Synergies of WO_3 and Co_3O_4 intercalated ball milling exfoliated graphene 3D helix electrocatalyst: A highly sensitive electrochemical detection of mesotrione herbicide in vegetable samples. *Food Chem.* **2024**, *432*, 137221.

[26] Kresse, G.; Furthmüller, J. Efficient iterative schemes for *ab initio* total-energy calculations using a plane-wave basis set. *Phys. Rev. B* **1996**, *54*, 11169–11186.

[27] Kresse, G.; Furthmüller, J. Efficiency of *ab-initio* total energy calculations for metals and semiconductors using a plane-wave basis set. *Comp. Mater. Sci.* **1996**, *6*, 15–50.

[28] Grimme, S.; Antony, J.; Ehrlich, S.; Krieg, H. A consistent and accurate *ab initio* parametrization of density functional dispersion correction (DFT-D) for the 94 elements H–Pu. *J. Chem. Phys.* **2010**, *132*, 154104.

[29] Shan, J. N.; Mo, G. M.; Chen, H. J.; Huangfu, Z. Y.; Huang, J.;

Ouyang, Q.; Huang, Q. Fabrication of SiAlCNO and SiAlC fibers from a photo-sensitive polyvinylaluminocarbosilane precursor using the ultraviolet curing method. *J. Am. Ceram. Soc.* **2025**, *108*, e20613.

[30] Wei, J. S.; Lu, X. H.; Lin, H. X.; Liu, S. Q.; Wei, X. X.; Sun, M.; Liu, G.; Hu, C. Z.; Wang, L. J.; Zhao, H. Z. et al. Coupling iron oxide with iron single-atom catalyst promotes neutral electrochemical nitrate reduction from water. *Water Res.* **2026**, *289*, 124936.

[31] Navik, R.; Tan, H. J.; Liu, Z. Y.; Xiang, Q. X.; Zhao, Y. P. Scalable production of high-quality exfoliated graphene using mechanical milling in conjugation with supercritical CO_2. *FlatChem* **2022**, *33*, 100374.

[32] Nguyen, T. H.; Tran, P. K. L.; Tran, D. T.; Pham, T. N.; Kim, N. H.; Lee, J. H. Single (Ni, Fe) atoms and ultrasmall core@shell Ni@Fe nanostructures dual-implanted CNTs-graphene nanonetworks for robust Zn-and Al-air batteries. *Chem. Eng. J.* **2022**, *440*, 135781.

[33] Xu, Z. J.; Wu, J. L.; Chen, W. H.; Jiang, Z. Q.; Cao, J.; Chen, G. L.; Jiang, Z. J. Plasma-assisted nitridation modulates the electronic structure of the $NiSe_2$/Ni@Ni_3N ternary heterojunction enhancing its dual-function catalytic performance and inhibiting Zn dendrite growth in rechargeable zinc-air batteries. *Adv. Funct. Mater.* **2025**, *35*, e11117.

[34] Xu, K. B.; Zou, R. J.; Li, W. Y.; Xue, Y. F.; Song, G. S.; Liu, Q.; Liu, X. J.; Hu, J. Q. Self-assembling hybrid NiO/Co_3O_4 ultrathin and mesoporous nanosheets into flower-like architectures for pseudocapacitance. *J. Mater. Chem. A* **2013**, *1*, 9107–9113.

[35] Kolathodi, M. S.; Palei, M.; Natarajan, T. S. Electrospun NiO nanofibers as cathode materials for high performance asymmetric supercapacitors. *J. Mater. Chem. A* **2015**, *3*, 7513–7522.

[36] Sun, X.; He, Y. Z.; Wang, M. F.; Cheng, Q. Y.; Huan, Y. F.; Liu, S. S.; Liu, J.; Qian, T.; Yan, C. L.; Lu, J. M. Maximizing available active hydrogen on FeNi substitutional solid-solution alloy to boost electrosynthesis of ammonia from nitrate. *ACS Nano* **2025**, *19*, 8189–8199.

[37] Lin, H. X.; Wei, J. S.; Guo, Y.; Li, Y.; Lu, X. H.; Zhou, C. C.; Liu, S. Q.; Li, Y. Y. Bi_1-$CuCo_2O_4$ hollow carbon nanofibers boosts NH_3 production from electrocatalytic nitrate reduction. *Adv. Funct. Mater.* **2024**, *34*, 2409696.

[38] Feng, C.; Wu, H. Y.; Shao, J. X.; Huo, Q. H.; Hassan, A.; Yang, H. P.; Hu, Q.; He, C. X. Sub-nanometer-scale Cu_9S_5 enables efficiently electrochemical nitrate reduction to ammonia. *Adv. Energy Mater.* **2025**, *15*, 2403354.

[39] Li, Y.; Wei, J. S.; Lin, H. X.; Guo, Y.; Lu, X. H.; Liu, S. Q.; Liu, H. Z.; Tang, M. Y.; Zhou, J.; Li, Y. Y. Hollow square Ni-doped copper oxide catalyst boosting electrocatalytic nitrate reduction. *ACS Catal.* **2025**, *15*, 1672–1683.

[40] Du, Y.; Lu, H. J.; Wu, J. T.; Zou, Y. L.; Huang, Z. F.; Zou, J. J.; Mu, T. S.; Gao, J.; Zhu, X. D.; Zhang, Y. C. Selenium-deficient $FeSe_2$/Fe_3O_4 electrocatalyst for nitrate reduction to ammonia. *Angew. Chem., Int. Ed.* **2025**, *64*, e202420903.

[41] Zhang, Z. J.; Ge, B. C.; Liu, M. R.; Yang, T. F.; Wang, S. T.; Liu, Y.; Yang, Y. J.; Gao, S. Y. Synergistic Cu_2O@$Ni(OH)_2$ core–shell electrocatalyst for high-efficiency nitrate reduction to ammonia. *ACS Appl. Mater. Interfaces* **2025**, *17*, 26501–26510.

[42] Liu, Y.; Niu, S. Y.; Zou, Y.; Huang, S. L.; Shi, Y. X.; Gao, S. Y.; Tsiakaras, P. Electrochemical production of ammonia: Nitrate reduction over novel Cu-Ni-Al metallic glass nanoparticles used as highly active and durable catalyst. *Appl. Catal. B: Environ. Energy* **2025**, *363*, 124729.

[43] Li, Z. Y.; Zheng, M.; Yan, C. S.; Yang, D. Q.; Yang, R. Y.; Zhang, C.; Liu, H. J.; Song, P.; Yin, C. H.; Qi, Z. M. et al. Stabilizing Cu^0–$Cu^{\delta+}$ sites via ohmic contact interface engineering for ampere-level nitrate electroreduction to ammonia. *Nat. Commun.* **2025**, *16*, 8940.

[44] Rinawati, M.; Chiu, Y. S.; Chang, L. Y.; Chang, C. Y.; Su, W. N.; Septiani, N. L. W.; Yuliarto, B.; Huang, W. H.; Chen, J. L.; Yeh, M. H. Evoking dynamic Fe–N_x active sites through the immobilization of molecular Fe catalysts on N-doped graphene quantum dots for the efficient electroreduction of nitrate to ammonia. *J. Mater. Chem. A* **2024**, *12*, 22070–22081.

[45] Shi, X. Y.; Xie, M. H.; Yang, K. W.; Niu, Y. T.; Ma, H. B.; Zhu, Y. M.; Li, J. Y.; Pan, T. T.; Zhou, X. Y.; Cui, Y. J. et al. Synergistic effect of Ni/$Ni(OH)_2$ core–shell catalyst boosts tandem nitrate reduction for ampere-level ammonia production. *Angew. Chem.* **2024**, *136*, e202406750.

[46] Huang, X. H.; Liu, Z. Y.; Yang, H. Y.; Ding, T.; Zhang, Z. H.; Yue, D. T.; Shi, G. S. Efficient electrocatalytic nitrate reduction to ammonia at low voltage through copper and graphene oxide co-modified nickel foam. *J. Power Sources* **2025**, *640*, 236748.

[47] Yang, J. Y.; Zhang, W. D.; Zhao, H.; Zou, Y. Z.; Zhang, Z. Y.; Liu, J. Y.; Wang, J.; Gu, Z. G.; Yan, X. D. High-valent cobalt active sites derived from electrochemical activation of metal-organic frameworks for efficient nitrate reduction to ammonia. *Appl. Catal. B: Environ.* **2024**, *340*, 123237.